Giant optical anisotropy in a quasi-one-dimensional crystal

Shanyuan Niu [1,9], Graham Joe[2,9], Huan Zhao [3,9], Yucheng Zhou[1], Thomas Orvis[1], Huaixun Huyan[1], Jad Salman[2], Krishnamurthy Mahalingam[4], Brittany Urwin[4], Jiangbin Wu[3], Yang Liu[1], Thomas E. Tiwald[5], Stephen B. Cronin[3], Brandon M. Howe[4], Matthew Mecklenburg[6], Ralf Haiges[7], David J. Singh[8], Han Wang[1,3]*, Mikhail A. Kats[2]* and Jayakanth Ravichandran[1,3]*

Optical anisotropy is a fundamental building block for linear and nonlinear optical components such as polarizers, wave plates, and phase-matching elements[1–4]. In solid homogeneous materials, the strongest optical anisotropy is found in crystals such as calcite and rutile[5,6]. Attempts to enhance anisotropic light–matter interaction often rely on artificial anisotropic micro/nanostructures (form birefringence)[7–11]. Here, we demonstrate rationally designed, giant optical anisotropy in single crystals of barium titanium sulfide ($BaTiS_3$). This material shows an unprecedented, broadband birefringence of up to 0.76 in the mid- to long-wave infrared, as well as a large dichroism window with absorption edges at 1.6 μm and 4.5 μm for light with polarization along two crystallographic axes on an easily accessible cleavage plane. The unusually large anisotropy is a result of the quasi-one-dimensional structure, combined with rational selection of the constituent ions to maximize the polarizability difference along different axes.

The nature of light propagation in an anisotropic system can be described by complex refractive indices ($n + i\kappa$) along the principal axes of the system. The optical anisotropy in a material can be quantified by the differences between the real parts of these indices as birefringence (Δn) and between the imaginary parts of the indices as dichroism ($\Delta \kappa$). Birefringence and/or dichroism are regularly found in inorganic crystals[5,6,12–16], liquid crystals[17–19], and engineered form-birefringent structures such as plasmonic arrays[7] and multi-slotted nanophotonic structures[10]. Currently, inorganic solids widely used for high-performance polarizing optics have a maximum birefringence of ~0.3 (refs [5,6,12–14,20,21]). Liquid crystals typically have birefringence below 0.4 (ref. [17]), although careful designs such as connecting multiple aromatic rings have achieved birefringence of up to 0.73 (ref. [18]). However, these bulky molecules are difficult to synthesize and use[19]. Anisotropic metamaterial or metasurface architectures with form birefringence can offer large optical anisotropy, but their use remains limited due to optical losses and fabrication challenges[7,22]. Hence, it is of scientific and technological importance to design thermodynamically stable homogeneous materials with large, easily accessible anisotropy for compact optical components.

Layered materials such as graphite and transition metal dichalcogenides are highly anisotropic due to differences between their interlayer and intralayer bonding[23,24]. However, the optic axis of these layered materials is typically the c axis, and it is difficult to access the a–c plane with large anisotropy. Recently, black phosphorus with lower-symmetry individual layers and easily accessible in-plane anisotropy has attracted considerable attention due to its anisotropy in vibrational, optical and electrical properties[25–28]. Nevertheless, the birefringence and dichroism in the a–b plane of black phosphorus remain modest[27], and its two-dimensional nature limits its utility in conventional optical systems.

Among various crystal structures, one can achieve large and accessible in-plane anisotropy in quasi-one-dimensional (quasi-1D) materials, where atoms are arranged in parallel chain-like structures. These rigid chains running along a high-symmetry principal axis ensure the optic axis is in a cleavage plane, which naturally reveals the large in-plane anisotropy between the intrachain and interchain directions. However, achieving large optical anisotropy even in such structurally anisotropic materials has remained a challenge[29]. The Clausius–Mossotti relation, which describes the relationship between the refractive index of a homogeneous medium and the polarizability of its constituent atoms, ions or molecules[30], provides a clue to solving this problem. Intuitively, one can achieve large optical anisotropy in quasi-1D materials by tuning the anisotropy of the polarizability tensor, which requires controlling the nature and distribution of the constituent elements. We looked to engineer the polarizability tensor of quasi-1D materials that crystallize in a hexagonal $BaNiO_3$-type structure (shown in Fig. 1a). These materials possess a general chemical formula, ABX_3, where A is typically an alkaline earth or alkali metal ion, and B is a transition metal ion surrounded by six anions (X). BX_6 octahedra sharing common faces are connected to form parallel chains along the c axis, which is the six-fold rotation axis and the optic axis of the material. The electronic polarizability of some of the candidate ions[30] for this structure are shown in Fig. 1d. Notably, the polarizability of S^{2-} (10.2 Å³) is much higher than that of O^{2-} (3.88 Å³) and is comparable to that of Se^{2-} (10.5 Å³). Ti^{4+}, with the lowest electronic polarizability among tetravalent transition

¹Mork Family Department of Chemical Engineering and Materials Science, University of Southern California, Los Angeles, CA, USA. ²Department of Electrical and Computer Engineering, University of Wisconsin–Madison, Madison, WI, USA. ³Ming Hsieh Department of Electrical Engineering, University of Southern California, Los Angeles, CA, USA. ⁴Materials and Manufacturing Directorate, Air Force Research Laboratory, Wright-Patterson AFB, Dayton, OH, USA. ⁵J. A. Woollam Co. Inc., Lincoln, NE, USA. ⁶Center for Electron Microscopy and Microanalysis, University of Southern California, Los Angeles, CA, USA. ⁷Loker Hydrocarbon Research Institute and Department of Chemistry, University of Southern California, Los Angeles, CA, USA. ⁸Department of Physics and Astronomy, University of Missouri, Columbia, MO, USA. ⁹These authors contributed equally: Shanyuan Niu, Graham Joe, Huan Zhao.
*e-mail: han.wang.4@usc.edu; mkats@wisc.edu; jayakanr@usc.edu
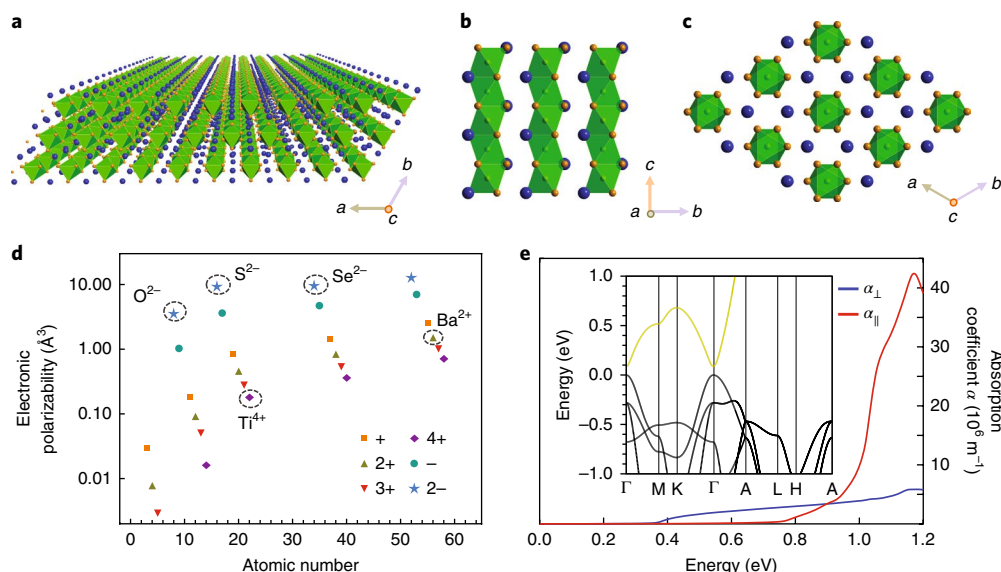
Fig. 1 | Structure and chemistry of BaTiS₃. a, Perspective view of a BaTiS$_3$ crystal plate with blue and orange spheres representing barium and sulfur atoms, respectively. TiS$_6$ octahedra are highlighted in green. **b**, BaTiS$_3$ crystal structure viewed along the a axis, showing TiS$_6$ chains parallel to the c axis. Green spheres represent titanium atoms. **c**, BaTiS$_3$ crystal structure viewed along the c axis, showing hexagonal symmetry. **d**, Electronic polarizabilities of selected candidate ions for the quasi-1D structure, plotted against the atomic number. The symbols classify the ions based on their typical valence, as noted in the legend, and the dashed circles highlight ions of elements relevant to the current study. **e**, Calculated absorption-coefficient spectra for light polarized parallel (red) and perpendicular (blue) to the c axis. The inset shows a calculated electronic band structure of BaTiS$_3$, with the titanium d_{z^2} band highlighted in gold. Γ, M, K, A, L and H represent the critical k-points in the Brillouin zone.

metal ions, and Ba^{2+}, with the highest value among common bivalent metal cations, are a good combination to offer a large polarizability difference between the c axis and a/b axes. Thus, we chose BaTiS$_3$ as a model system among this class of quasi-1D materials to demonstrate large optical anisotropy via 'chemical polarizability engineering' (discussions in Supplementary Section 8).

BaTiS$_3$ is uniaxial with diagonal dielectric tensor elements, $\varepsilon_{aa} = \varepsilon_{bb} \neq \varepsilon_{cc}$. We denote the two different components of the tensor with electric field perpendicular ($\varepsilon_\perp = \varepsilon_{aa}$) and parallel ($\varepsilon_\parallel = \varepsilon_{cc}$) to the c axis. We performed density-functional calculations to verify the proposed heuristic selection process. The calculations yielded pronounced anisotropic optical properties and a large, broadband linear dichroism window. Calculated absorption coefficients for light polarized parallel ($\alpha_\parallel$) and perpendicular ($\alpha_\perp$) to the c axis are shown in Fig. 1e. Here, $\alpha_\parallel$ shows a prominent absorption edge, while $\alpha_\perp$ extends to lower energies. The calculated values of the absorption edges are sensitive to the approximations used to include correlation effects of titanium d orbitals (more details in Methods and Supplementary Section 6). Irrespective of the parameters used, two distinct absorption edges in $\alpha_\parallel$ and $\alpha_\perp$ were observed. The origin of the anisotropic absorption edges can be understood by analysing the band structure with dipole-transition selection rules, and has been discussed for similar hexagonal structures[31]. Note that the true fundamental band gap can be lower than the optical absorption edges seen here (discussions in Supplementary Section 6).

Large single-crystal platelets of BaTiS$_3$ with lateral dimensions of several millimetres were grown by the vapour transport method with iodine as a transport agent. We encountered two predominant morphologies: needle-like and platelet-like crystals (Fig. 2a). Scanning electron microscopy (SEM) images of these crystals (Fig. 2b,d) show smooth crystal faces. We performed single-crystal X-ray diffraction studies and found that they adopted the $P6_3mc$ space group (complete structural parameters are in Supplementary Section 7), which agrees with previous structural studies[32–34]. A thin-film out-of-plane X-ray diffraction scan of the crystal plate is shown in Fig. 2c. The presence of sharp 100-type reflections

proves that the crystal face has {100} orientation with the c axis in-plane. We identified the c axis by confirming its six-fold rotational symmetry (Supplementary Fig. 1). Energy-dispersive X-ray spectroscopy (EDS) mapping showed the expected composition (Supplementary Fig. 5), as well as uniform distribution of all elements (Fig. 2d). We performed polarization-resolved Raman spectroscopy and observed pronounced anisotropic vibrational properties of this quasi-1D lattice (Fig. 2e, Supplementary Section 3 and Supplementary Fig. 4). High-angle annular dark-field scanning transmission electron microscopy (STEM) images of the crystals along the a axis (Fig. 2f) and c axis (Fig. 2g) clearly reveal the presence of parallel 1D chains along the c axis and the hexagonal arrangement of the chains. Selected-area electron diffraction patterns are available in Supplementary Figs. 2 and 3.

Polarization-resolved infrared spectroscopy was performed to obtain the transmission and reflection spectra, with incident light polarized parallel and perpendicular to the c axis (Fig. 3a,b). The thickness of the plate was estimated to be 13 μm by fitting to the Fabry–Pérot fringes in the spectra. When the polarization was perpendicular to the c axis, the absorption edge was observed at 4.5 μm (0.27 eV). However, when the polarization was parallel to the c axis, the absorption edge was blueshifted to 1.6 μm (0.76 eV). The reflection spectra are consistent with the transmission spectra as the fringes vanish at wavelengths corresponding to the two different absorption edges. To fully quantify the degree of optical anisotropy, we performed generalized ellipsometry measurements over the spectral range of 210 nm to 1,500 nm for several sample orientations. By combining these measurements with the polarization-resolved transmission and reflection measurements in Fig. 3a,b, we extracted the optical properties of BaTiS$_3$ over the 210 nm to 16 μm wavelength range (Supplementary Section 5, Supplementary Figs. 6–8). The real (ε_1) and imaginary (ε_2) parts of the diagonalized dielectric tensor over the entire measured range are plotted in Fig. 3c. The extracted wavelength-dependent birefringence ($\Delta n = n_\parallel - n_\perp$), linear dichroism ($\Delta \kappa = \kappa_\parallel - \kappa_\perp$) and normalized dichroism ($\eta = \frac{(\kappa_\parallel - \kappa_\perp)}{(\kappa_\parallel + \kappa_\perp)}$) are shown in Fig. 3d. The normalized dichroism is near unity in the
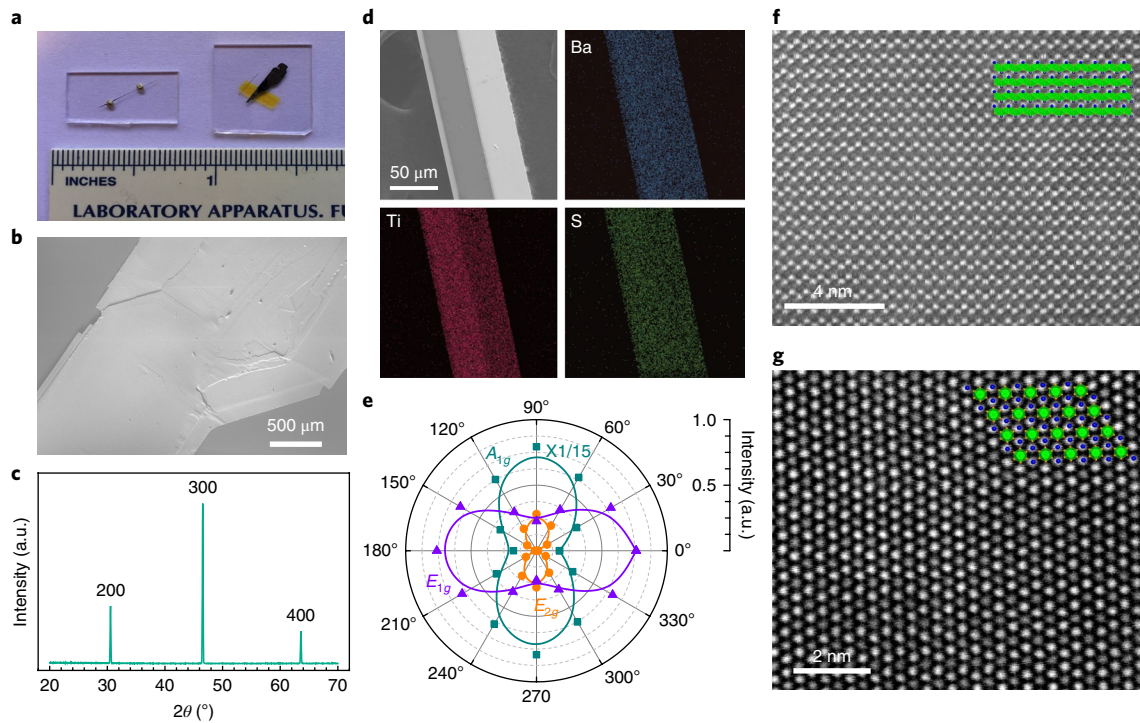
Fig. 2 | Structural, vibrational and chemical characterization of BaTiS₃. a, Optical image of the representative as-grown $BaTiS_3$ crystal needle and plate. The needle is clamped down on the glass substrate by two silver paint dots. **b**, SEM image of a $BaTiS_3$ plate. The scale bar is 500 μm. **c**, Out-of-plane X-ray diffraction scan of a $BaTiS_3$ plate; a.u. are arbitrary units. **d**, EDS mapping of barium (blue), titanium (red) and sulfur (green) elements on a $BaTiS_3$ crystal needle (top left). The scale bar is 50 μm. **e**, Intensity of three Raman modes, E_{2g}, E_{1g} and A_{1g}, of $BaTiS_3$ at 183 cm⁻¹, 187 cm⁻¹ and 380 cm⁻¹, respectively, with different excitation laser polarizations plotted in polar coordinates; 0° refers to the polarization perpendicular to the c axis. The intensity of the A_{1g} mode is scaled down by a factor of 15 (indicated by 'X1/15'). **f,g**, High-angle annular dark-field STEM images of $BaTiS_3$ viewed along the a axis (**f**) and c axis (**g**). The insets are corresponding schematic crystal structures overlaid with the STEM images. The scale bars in **f** and **g** are 4 nm and 2 nm, respectively.
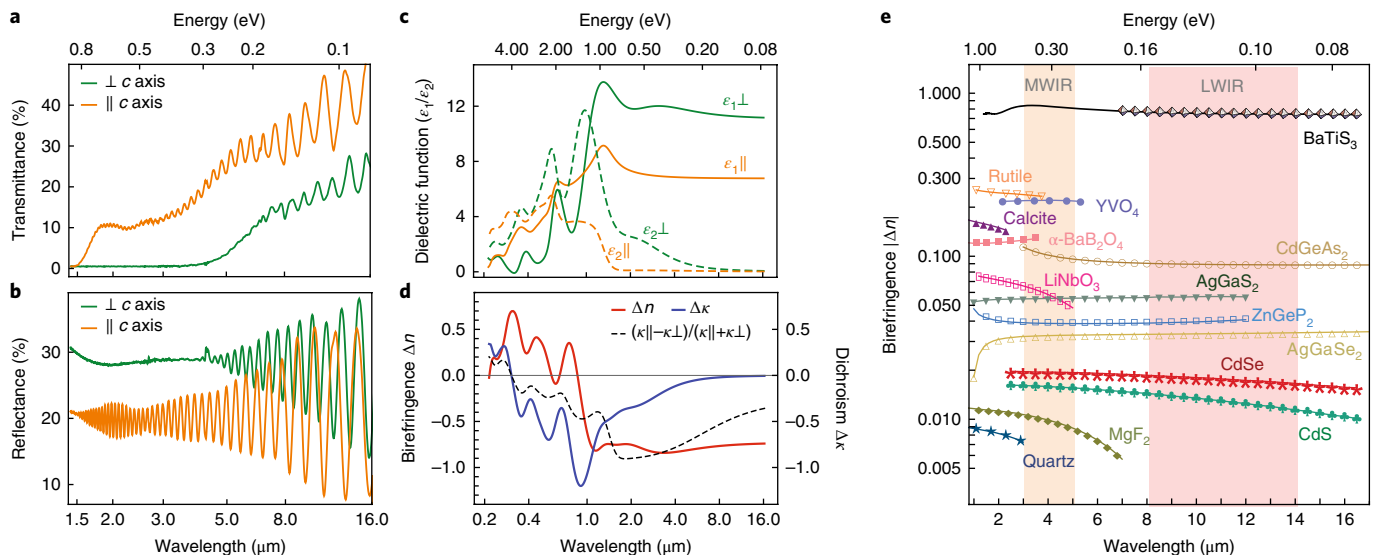
Fig. 3 | Optical anisotropy. a,b, Infrared transmission (**a**) and reflection (**b**) spectra for incident light polarized perpendicular (dark green) and parallel (orange) to the c axis. **c**, Real (ε_1) and imaginary (ε_2) parts of the dielectric function for polarization perpendicular and parallel to the c axis, extracted from a combination of ellipsometry and polarization-resolved transmission/reflectance measurements. **d**, Birefringence ($\Delta n = n_\parallel - n_\perp$), linear dichroism ($\Delta \kappa = \kappa_\parallel - \kappa_\perp$) and normalized dichroism $\eta = \frac{(\kappa_\parallel - \kappa_\perp)}{(\kappa_\parallel + \kappa_\perp)}$ for wavelengths from 210 nm to 16 μm. **e**, A comparison of absolute birefringence values for various birefringent materials and $BaTiS_3$ in the infrared. The fully transparent region of $BaTiS_3$ is indicated by octahedra symbols. Mid-infrared atmospheric transparency regions (mid-wave infrared (MWIR) and long-wave infrared (LWIR)) are highlighted. The birefringence values for other materials in **e** were adopted from several reports[5,6,12–16,35].

strongly dichroic window of 1.5–4.5 µm, and significant dichroism persists up to the visible range and changes sign at 300 nm. The transparent region for BaTiS$_3$ starts at ~8 µm and persists to the longest measured wavelength, 16.7 µm. We emphasize that in this low-loss region, the material displays an unprecedented birefringence magnitude of up to 0.76, which is higher than the current largest birefringence in liquid crystals and more than twice as large as 0.29 in rutile[6]. To the best of our knowledge, this is the highest reported birefringence among anisotropic crystals, and is an order of magnitude larger than widely used long-wave infrared birefringent materials (Fig. 3e). BaTiS$_3$ possesses broadband, giant birefringence over the entire infrared spectrum, covering the short-wave infrared, mid-wave infrared and long-wave infrared atmospheric transmission windows.

In conclusion, we have rationally designed and realized a material, BaTiS$_3$, that features an unprecedented degree of optical anisotropy. This anisotropy is achieved in an easily accessible crystal plane and is enabled by the quasi-1D hexagonal perovskite structure of BaTiS$_3$, coupled with a judicious selection of the constituent ions (chemical polarizability engineering). We synthesized large single-crystal plates of BaTiS$_3$ and fully characterized the refractive-index tensor from the ultraviolet to the long-wave infrared. BaTiS$_3$ crystals possess a broadband dichroism window and giant birefringence of up to 0.76, more than double the value in any other transparent homogeneous solid (to the best of our knowledge). We anticipate BaTiS$_3$ and other quasi-1D materials will be broadly useful for next-generation imaging, communications and sensing applications, especially for miniaturized photonic devices. We also expect these materials to possess large anisotropies in electrical, thermal and other physical properties, further expanding their scientific and technological importance.

Methods

Methods, including statements of data availability and any associated accession codes and references, are available at https://doi.org/10.1038/s41566-018-0189-1.

References

1. Yasuno, Y., Makita, S., Sutoh, Y., Itoh, M. & Yatagai, T. Birefringence imaging of human skin by polarization-sensitive spectral interferometric optical coherence tomography. *Opt. Lett.* **27**, 1803–1805 (2002).
2. Weber, M. F. Giant birefringent optics in multilayer polymer mirrors. *Science* **287**, 2451–2456 (2000).
3. Oka, K. & Kaneko, T. Compact complete imaging polarimeter using birefringent wedge prisms. *Opt. Express* **11**, 1510–1519 (2003).
4. Nicholls, L. H. et al. Ultrafast synthesis and switching of light polarization in nonlinear anisotropic metamaterials. *Nat. Photon.* **11**, 628–633 (2017).
5. Ghosh, G. Dispersion-equation coefficients for the refractive index and birefringence of calcite and quartz crystals. *Opt. Commun.* **163**, 95–102 (1999).
6. Sinton, W. M. Birefringence of rutile in the infrared. *J. Opt. Soc. Am.* **51**, 1309–1310 (1961).
7. Kats, M. A. et al. Giant birefringence in optical antenna arrays with widely tailorable optical anisotropy. *Proc. Natl Acad. Sci. USA* **109**, 12364–12368 (2012).
8. Yu, N. & Capasso, F. Flat optics with designer metasurfaces. *Nat. Mater.* **13**, 139–150 (2014).
9. Larouche, S., Tsai, Y.-J., Tyler, T., Jokerst, N. M. & Smith, D. R. Infrared metamaterial phase holograms. *Nat. Mater.* **11**, 450–454 (2012).
10. Yang, S.-H., Cooper, M. L., Bandaru, P. R. & Mookherjea, S. Giant birefringence in multi-slotted silicon nanophotonic waveguides. *Opt. Express* **16**, 8306–8316 (2008).
11. Zheludev, N. I. & Kivshar, Y. S. From metamaterials to metadevices. *Nat. Mater.* **11**, 917–924 (2012).
12. Luo, H. T., Tkaczyk, T., Dereniak, E. L., Oka, K. & Sampson, R. High birefringence of the yttrium vanadate crystal in the middle wavelength infrared. *Opt. Lett.* **31**, 616–618 (2006).
13. Zelmon, D. E., Small, D. L. & Jundt, D. Infrared corrected Sellmeier coefficients for congruently grown lithium niobate and 5 mol.% magnesium oxide–doped lithium niobate. *J. Opt. Soc. Am. B* **14**, 3319–3322 (1997).
14. Guoqing, Z. et al. Growth and spectrum of a novel birefringent α-BaB$_2$O$_4$ crystal. *J. Cryst. Growth* **191**, 517–519 (1998).
15. Chenault, D. B. & Chipman, R. A. Infrared birefringence spectra for cadmium sulfide and cadmium selenide. *Appl. Opt.* **32**, 4223–4227 (1993).
16. Dodge, M. J. Refractive properties of magnesium fluoride. *Appl. Opt.* **23**, 1980–1985 (1984).
17. Sekine, C., Iwakura, K., Konya, N., Minai, M. & Fujisawa, K. Synthesis and properties of some novel high birefringence phenylacetylene liquid crystal materials with lateral substituents. *Liq. Cryst.* **28**, 1375–1387 (2001).
18. Herman, J. & Kula, P. Design of new super-high birefringent isothiocyanato bistolanes—synthesis and properties. *Liq. Cryst.* **44**, 1462–1467 (2017).
19. Węgłowska, D., Kula, P. & Herman, J. High birefringence bistolane liquid crystals: synthesis and properties. *RSC Adv.* **6**, 403–408 (2016).
20. Zhang, H. et al. Na$_3$Ba$_2$(B$_3$O$_6$)$_2$F: next generation of deep-ultraviolet birefringent materials. *Cryst. Growth Des.* **15**, 523–529 (2014).
21. Jia, Z. et al. Top-seeded solution growth and optical properties of deep-UV birefringent crystal Ba$_2$Ca(B$_3$O$_6$)$_2$. *Cryst. Growth Des.* **17**, 558–562 (2017).
22. Zhang, W., Liu, J., Huang, W.-P. & Zhao, W. Giant birefringence of periodic dielectric waveguides. *IEEE Photonics J.* **3**, 512–520 (2011).
23. Geim, A. K. & Novoselov, K. S. The rise of graphene. *Nat. Mater.* **6**, 183–191 (2007).
24. Wang, Q. H., Kalantar-Zadeh, K., Kis, A., Coleman, J. N. & Strano, M. S. Electronics and optoelectronics of two-dimensional transition metal dichalcogenides. *Nat. Nanotech.* **7**, 699–712 (2012).
25. Xia, F., Wang, H. & Jia, Y. Rediscovering black phosphorus as an anisotropic layered material for optoelectronics and electronics. *Nat. Commun.* **5**, 4458 (2014).
26. Wang, X. Highly anisotropic and robust excitons in monolayer black phosphorus. *Nat. Nanotech.* **10**, 517–521 (2015).
27. Mao, N. et al. Optical anisotropy of black phosphorus in the visible regime. *J. Am. Chem. Soc.* **138**, 300–305 (2016).
28. Liao, B. et al. Spatial-temporal imaging of anisotropic photocarrier dynamics in black phosphorus. *Nano Lett.* **17**, 3675–3680 (2017).
29. Iio, K., Hyodo, H. & Nagata, K. Observations of short-range order by optical birefringence in one-dimensional antiferromagnets CsNiCl$_3$, RbNiCl$_3$ and CsCoCl$_3$. *J. Phys. Soc. Jpn* **49**, 1336–1343 (1980).
30. Rumble, J. (ed.) *CRC Handbook of Chemistry and Physics* 98th edn (CRC Press, Boca Raton, 2017).
31. Huang, X., Paudel, T. R., Dong, S. & Tsymbal, E. Y. Hexagonal rare-earth manganites as promising photovoltaics and light polarizers. *Phys. Rev. B* **92**, 125201 (2015).
32. Hahn, H. & Mutschke, U. Untersuchungen über ternäre Chalkogenide. XI. Versuche zur Darstellung von Thioperowskiten. *Z. Anorg. Allg. Chem.* **288**, 269–278 (1957).
33. Clearfield, A. The synthesis and crystal structures of some alkaline earth titanium and zirconium sulfides. *Acta Cryst.* **16**, 135–142 (1963).
34. Huster, J. Die Kristallstruktur von BaTiS$_3$. *Z. Naturforsch. B* **35**, 775 (1980).
35. Nikogosyan, D. N. *Nonlinear Optical Crystals: A Complete Survey* (Springer-Verlag, New York, 2005).

Author contributions

J.R. conceived and supervised the research with M.A.K. M.A.K. identified the large optical anisotropy. H.W. supervised the Raman and infrared spectroscopy studies. S.N., Y.Z. and H.H. built the apparatus and grew the crystals. S.N., Y.L. and T.O. performed structural and chemical characterizations. R.H. contributed single-crystal

X-ray diffraction measurements. M.M., K.M., B.U. and B.M.H. contributed TEM studies. S.N., H.Z. and J.W. studied the Raman response. G.J., H.Z. and J.S. performed infrared spectroscopy. G.J. and T.E.T. performed ellipsometry studies. D.J.S. contributed theoretical calculations. All authors discussed the results. S.N., M.A.K. and J.R. wrote the manuscript with contributions from all authors.

Competing interests

The authors declare no competing interests.

Additional information

Methods

Synthesis. The synthesis method is similar to that used for other perovskite sulfides reported elsewhere[36]. Starting materials, barium sulfide powder (Sigma-Aldrich, 99.9%), titanium powder (Alfa Aesar, 99.9%), sulfur pieces (Alfa Aesar, 99.999%) and iodine pieces (Alfa Aesar 99.99%) were stored and handled in an argon-filled glove box. Stoichiometric quantities of precursor powders with a total weight of 0.5 g were mixed and loaded into a quartz tube of diameter 0.75 inch and thickness 1.5 mm along with around 0.5 mg cm^{-3} iodine inside the glove box. The tube was capped with ultra-torr fittings and a bonnet needle valve to avoid exposure to the air. The tube was then evacuated and sealed using a blowtorch, with oxygen and natural gas as the combustion mixture. The sealed tube was about 12 cm in length, and was heated to 1,000 °C with a 0.3 °C min^{-1} ramp rate and held at 1,000 °C for 60 h. The samples were quenched to room temperature after the dwell time using a sliding furnace setup with a cooling rate of ~100 °C min^{-1}.

X-ray diffraction. The thin-film out-of-plane X-ray diffraction scan and the X-ray diffraction map with sample tilt of the crystal plate were carried out in a Bruker D8 Advance X-ray diffractometer in parallel beam configuration, using a germanium (004) two-bounce monochromator for copper K$_{\alpha1}$ radiation. The map was taken for a 2θ range of 20° to 70° with steps of 0.025°, and a ψ range of 5° to 70° with steps of 0.5°. 2θ is the angle between the axes connecting the source and the goniometer, and the detector and the goniometer. ψ is the tilting axis of the goniometer with respect to the axis connecting the source and the detector. The single-crystal X-ray diffraction data were collected on a Bruker SMART APEX DUO three-circle platform diffractometer with the χ axis fixed at 50.74°, using monochromatic molybdenum K$_{\alpha}$ radiation (wavelength $\lambda = 0.71073$ Å). χ is the angle between the spindle axis of the goniometer head and the main instrument axis. The diffractometer was equipped with an APEX II CCD (charge-coupled device) detector and an Oxford Cryosystems Cryostream 700 apparatus for low-temperature data collection. A black needle-like specimen of BaTiS$_3$, approximate dimensions 0.044 mm × 0.060 mm × 0.512 mm, was used for the X-ray crystallographic analysis results in Supplementary Tables 2–7. The crystal was mounted in a Cryo-Loop using Paratone oil. A complete hemisphere of data were scanned on omega (0.5°) at a detector distance of 50 mm and a resolution of 512 × 512 pixels. A total of 2,520 frames were collected.

SEM and EDS. SEM images were obtained in a JEOL JEM-7001F analytical field-emission scanning electron microscope equipped with EDAX Apollo X 10 mm^2 EDS. All SEM images and EDS spectra were acquired with settings of 15 kV accelerating voltage, around 67 μA emission current and a working distance of 15 mm. Magnifications from ×100 to ×15,000 were used for the EDS spectra, and the obtained chemical composition ratios were consistent between these magnifications. A representative spectrum recorded at ×400 is in Supplementary Fig. 5.

STEM. The image in Fig. 2f was acquired on the JEOL JEM-300CF (Grand ARM) transmission electron microscope (TEM) at the Irvine Materials Research Institute at the University of California, Irvine. The STEM data were acquired at an accelerating voltage of 300 kV, a beam current of 20 pA and a probe semiconvergence angle of 28 mrad. The image resolution in Fig. 2f is roughly 80 pm. The samples were prepared using standard focused ion beam milling liftout techniques at the University of California Los Angeles using an FEI Nova 600 Nanolab equipped with FEI's Magnum gallium focused ion beam column. The final gallium ion polish on the sample was done with an accelerating voltage of 10 kV. The diffraction pattern is in Supplementary Fig. 3 and was acquired on a JEOL JEM-2100F at the University of Southern California's Center for Electron Microscopy and Microanalysis. The image in Fig. 2g was acquired using a TalosTM (ThermoFisher Scientific) TEM operated at an accelerating voltage of 200 kV. Samples for TEM observations were prepared by focused ion beam milling using a gallium ion beam at an accelerating voltage of 30 kV, followed by a cleaning/polishing procedure by argon ion milling at 1.5 kV and 700 V to remove focused-ion-beam-induced residual gallium and surface amorphization in the sample.

Raman spectroscopy. Polarization-resolved Raman spectroscopy was performed in a Renishaw inVia confocal Raman Microscope with a 532 nm

laser and a ×100 microscope objective at room temperature. The polarization of the incident beam was controlled by a rotating half-wave plate in the incident beam path. No polarizing optics were used in the detection beam path.

Infrared reflection/transmission spectroscopy. Polarization-resolved infrared spectroscopy was carried out using a Fourier transfer infrared spectrometer (Bruker Optics Vertex 70) and an infrared microscope (Hyperion 2000). A 15× Cassegrain microscope objective (numerical aperture = 0.4) was used for both transmission and reflection measurements at normal incidence on the (100) face of a BaTiS$_3$ crystal plate mounted on a TEM grid with a hole diameter of 200 μm, to avoid any spurious effects due to the substrate. In the case of transmission measurements, two identical objectives were used. The polarization of the incident light beam was controlled using a wire-grid polarizer for the mid-infrared spectral range and a nanoparticle polarizer for the visible to near-infrared spectral range. Mid-infrared measurements were performed with a Globar source, a potassium bromide beam splitter and a mercury cadmium telluride detector. Visible and short near-infrared measurements were performed with a halogen lamp source, quartz beam splitter and silicon photodetector. The intermediate spectral range was measured with the halogen lamp source, quartz beam splitter and mercury cadmium telluride detector. In this paper, measurements from different spectral ranges have been presented in a single figure.

Ellipsometry. Generalized ellipsometry was acquired using an RC2 ellipsometer and analysed with WVASE software (Woollam). The measurement was performed over a spectral range of 210 nm to 1,500 nm at an angle of incidence of 64.7°. Data were used from three different sample orientations (optic axis parallel, perpendicular and 14° to the plane of incidence) to back out the optical constants in this spectral range. The BaTiS$_3$ crystal plate was mounted on a glass substrate with silver epoxy, but the material was treated as infinitely thick since it is strongly absorbing in this spectral range. More details can be found in Supplementary Section 5 and Supplementary Figs. 6, 7 and 8.

Theoretical calculations. First-principles calculations were done using the general potential linearized augmented planewave (LAPW) method[37], as implemented in the WIEN2k code[38]. We used the experimental lattice parameters. The non-symmetry-constrained atomic coordinates were determined by structure relaxation using the standard Perdew–Burke–Ernzerhof potentials under generalized gradient approximation (GGA). The electronic structures and optical properties were then obtained using the standard Perdew–Burke–Ernzerhof GGA, the GGA + U method, where correlation effects beyond GGA are treated at a semi-empirical level within a rotationally invariant formalism, and the modified Becke–Johnson potential[39]. U refers to the Coulomb parameter. The representative data shown in Fig. 1 were obtained with a U value of 8 eV for titanium d orbitals. The corresponding data calculated with modified Becke–Johnson potential are in Supplementary Section 6 and Supplementary Fig. 9. We used highly converged basis sets determined by the criterion $R_{min}k_{max} = 9$ plus local orbitals and dense grids (up to 24 × 24 × 24) to sample the Brillouin zone. R_{min} is the smallest LAPW sphere radius and k_{max} is the planewave sector cutoff. Interband optical absorption was calculated using the optical package of WIEN2k.

Data availability. The data that support the results within this paper and other findings of this study are available from the corresponding authors upon reasonable request.

References

36. Niu, S. et al. Bandgap control via structural and chemical tuning of transition metal perovskite chalcogenides. *Adv. Mater.* **29**, 1604733 (2017).
37. Singh, D. J. & Nordstrom, L. (eds) *Planewaves, Pseudopotentials, and the LAPW Method* (Springer, New York, 2006).
38. Blaha, P., Schwarz, K., Madsen, G., Kvasnicka, D. & Luitz, J. *WIEN2k, An Augmented Plane Wave + Local Orbitals Program For Calculating Crystal Properties* (Technische Univ. Wien, Vienna, 2001).
39. Tran, F. & Blaha, P. Accurate band gaps of semiconductors and insulators with a semilocal exchange-correlation potential. *Phys. Rev. Lett.* **102**, 226401 (2009).